https://doi.org/10.5194/egusphere-2023-1758
Preprint. Discussion started: 8 August 2023

Impact of melt pond and floe size on the optical properties of Arctic sea ice

Hang Zhang[1], Miao Yu[1], Peng Lu[1*], Jiaru Zhou[1], Qingkai Wang[1], Zhijun Li[1]

[1] State Key Laboratory of Coastal and Offshore Engineering, Dalian University of Technology, Dalian 116024, China

Correspondence to: Peng Lu (lupeng@dlut.edu.cn)

Abstract. Melt ponds are usually modelled as horizontally infinite water layer overlaying on level ice. Then the albedo of summer Arctic sea ice can be determined by a linear combination of melt pond and bare ice albedo weighted by their areal coverage. However, this simulation does not reflect actual reality, in which ponds always have a limited size. In the present study, a Monte Carlo (MC) model was employed to investigate the influence of melt pond and floe size on the apparent optical properties of summer sea ice. The results showed that albedo and bottom transmittance mainly depended on the melt pond fraction (MPF) and ice thickness, respectively. The radiation absorbed by pond water depended on both pond depth and MPF. The radiation absorbed by ice depended on both pond depth and ice thickness. Two new parameters, the ratio of albedo (K_α) and transmittance (K_T) of the linear combination to the MC model, are proposed to present the accuracy of the linear combination. For small-sized floe, K_α and K_T decreased from 1.33 to 1.02 and from 3.96 to 1.05, respectively, as floe size increased from 2 to 40 m with an MPF of 50%. K_α increased from 1.10 to 2.00 as MPF increased from 0 to 100% with a floe size of 2 m. Solar radiation is more likely to penetrating into the lateral ocean in small floes than in large floes, and the small MPF, which has a high albedo, prevents solar energy from entering the floe. To reduce these uncertainties, new parameterization formulas for K_α and K_T at different latitudes and different melting stages are provided. In the marginal ice zone, the average K_α and K_T are about 1.03 and 1.12, respectively. During the melting season, the difference of K_α for MC model and linear combination could reach up to 34% with the ice size 2 m for first-year ice. The results of this study can be used in future research to correct in situ data obtained via linear combination for floe sizes smaller than 20 m.

1 Introduction

Melt ponds form on the Arctic sea ice surface in summer and are one of the most distinct characteristics of the Arctic (Polashenski et al., 2012). The maximum melt pond fraction (MPF) can reach 50% on the ice surface (Webster et al., 2015) and cause the albedo of Arctic sea ice to drop from 0.7 to 0.15 (Light et al., 2022; Grenfell and Perovich, 2004). Ponded ice can also absorb and transmit more solar energy than bare ice to promote melt and warm the Arctic sea ice (Nicolaus et al., 2012; Katlein et al., 2019). The formation of melt ponds generates a positive feedback mechanism that increases the absorption of solar radiation by sea ice and promotes its melting (Landy et al., 2015; Polashenski et al., 2012). Consequently, melt ponds play an extremely important role in the dramatic decay of Arctic sea ice (Flocco et al., 2012).

https://doi.org/10.5194/egusphere-2023-1758
Preprint. Discussion started: 8 August 2023

The apparent optical properties (AOPs) of melt ponds have been extensively investigated through field measurements and numerical simulations. Different factors on the melt pond AOPs had been simulated by Lu et al. (2018), and the parameterization of albedo and transmittance as function of pond depth (H_p) and underlying ice thickness (H_i) were investigated. The PAR transmittance of melt pond is twice larger than the white ice (Light et al., 2022), and the total transmittance of the ponded ice is about 4.4 times larger than that of bare ice due to the melting of surface scattering layer and drained layer of the bare ice (Light et al., 2015). Skyllingstad et al. (2009) simulated the solar irradiance transfer in the melt pond, and the variation in albedo with the bottom ice albedo and H_p were put forward. Furthermore, according to the two stream radiative transfer theory, the spectral albedo of melt pond can be determined based on H_p, and the pond bottom albedo (Malinka et al., 2018).

Most measurements and numerical simulations regarded H_p and H_i as the main factor of pond AOPs. Then, melt pond was assumed as a plane-parallel layer with infinite pure water in most models. Arctic sea ice albedo in summer is calculated through the linear combination of ice and melt pond (e.g., Zege et al., 2015; Istomina et al., 2015; Briegleb and Light, 2007). However, pond size can greatly affect the surface albedo. For the pond larger than 10 m, the measured spectral albedo is restricted to a constant value (in most cases lower than 0.1) for wavelengths longer than 900 nm (Light et al., 2015). However, in the pond size smaller than 1 m, the observed spectral albedo in the 1050 – 1110 nm has a peak (Polashenski et al., 2012), which indicates that also the albedo of surrounding sea ice or snow is being detected by the optical sensor (Malinka et al., 2018). Besides, the spectral albedo in the 800 – 920 nm measured by Cao et al. (2020) was larger than 0.2, which was obviously affected by the surrounded ice. The relative transmissivity, which is the ratio of transmittance with different ice size to the infinite medium, increases with the increase of ice size (Light et al., 2003). These studies have shown that the AOPs of small ponds are size-dependent and inevitably affected by the surrounding ice. This means that infinite parallel plane assumptions and linear combination method are not suitable for all situations.

The aim of this study was to explore the influence of floe and pond size on their optical properties such as surface albedo and bottom transmittance. To this end, a Monte Carlo (MC) model was developed to parameterize the optical properties of melt ponds. This paper is structured as follows: Section 2 introduces the MC model; Section 3 reports the results obtained, describing the influence of various factors, such as pond depth, underlying ice thickness, ice foe size, and the energy absorption rate of ice floe. Section 4 verifies the model and presents the parameterization for different latitudes and different melting stages to correct the ice floe' AOPs; and Section 5 summarizes the conclusions.

2 Methods

2.1 Model setup

A schematic diagram of the summer sea ice surface featuring a melt pond is shown in Figure 1. As this study focused mainly on the AOPs of melt pond and sea ice, the freeboard and hydraulic head of pond water above the sea level were ignored. The floe was assumed to be optically isotropic (Katlein et al., 2015), therefore, the shape of floe and melt pond were set as circle

https://doi.org/10.5194/egusphere-2023-1758
Preprint. Discussion started: 8 August 2023

with diameters defined as d_i and d_p (Figure 1). Their areas were calculated as $S_i = \pi d_i^2/4$ and $S_p = \pi d_p^2/4$, respectively. Then, the melt pond fraction (MPF) was expressed as MPF = S_p / S_i = $(d_i / d_p)^2$. In the following text, the size of pond or floe refers to its diameter. Based on the CICE model, the surrounding ice was divided into five layers: the surface scattering layer (SSL), drained layer (DL), and three interior layers (IL_i) (Briegleb and Light, 2007). Ice floe thickness was denoted by d. The thickness of IL_i was d/4. If $d < 1.5$ m, the thickness of SSL was d/30, and if $d \geq 1.5$ m, it was 0.05 m. The thickness of DL was d/4 – SSL. The ice beneath melt pond consists of only one interior layer (IL_p).

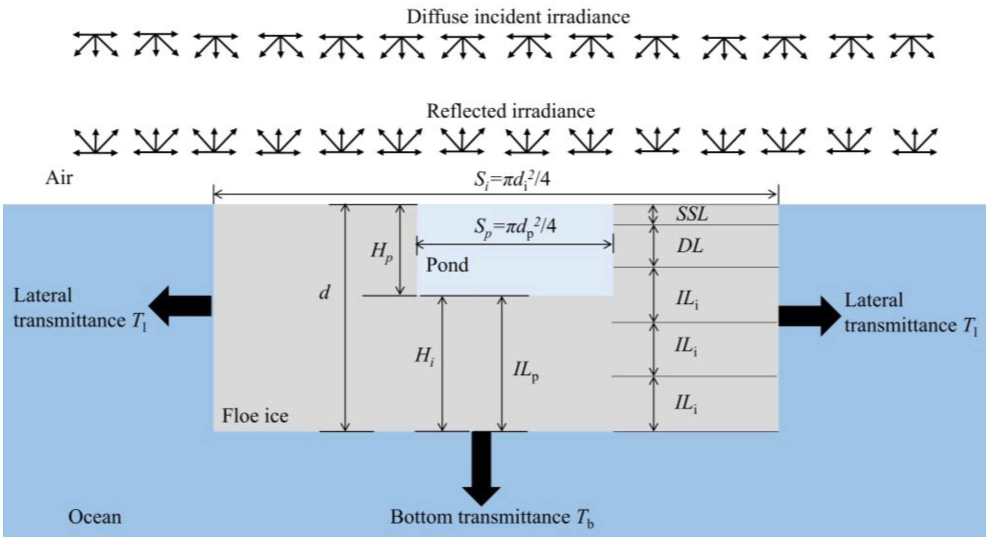

Figure 1: Schematic diagram of bare ice floe with a melt pond on the surface in summer. H_p is the melt pond depth, H_i is the underlying ice thickness, and d is the floe thickness. S_i and S_p are the floe and melt pond areas, respectively. SSL is the surface scattering layer, DL is the drained layer, IL_i is the interior layer of surrounding sea ice, and IL_p is the interior layer of ice beneath pond.

2.2 Monte Carlo model

The MC model is a random simulation method. Solar radiation reaching the medium surface consists of be infinitely narrow beams containing 10^6 photons. Each photon is described by six variables: 3D space position coordination (x, y, and z) and three direction cosines of the moving direction (u, v, and w). The initial weight of each photon is 1 ($W = 1$). The probability density function of the photon motion step L obeys Beer's law:

$$L = -\frac{ln\zeta}{\varepsilon} \quad (1)$$

where the parameter ζ is a random number uniformly distributed between 0 and 1, and ε is the extinction coefficient, namely the sum of absorption coefficient k and scattering coefficient σ. Once the step is determined, the position of the photon after the collision with the medium can be calculated as follows:

https://doi.org/10.5194/egusphere-2023-1758
Preprint. Discussion started: 8 August 2023

$$\begin{cases} x_{m+1} = x_m + Lu_{m+1} \\ y_{m+1} = y_m + Lv_{m+1} \\ z_{m+1} = z_m + Lw_{m+1} \end{cases} \quad (2)$$

The photon will undergo absorption during its movement. When it reaches the new position, a part of the weight, ΔW (k/ε), is absorbed by the medium. Then, this "lighter" photon starts a new scattering to generate the direction of the next movement. It should be noted that, once the photon reaches the lateral and bottom ocean, the weight decreases to 0. The new direction is controlled by the asymmetry parameter g. When g = 0, which means that the medium is isotropic, the azimuth angle φ is evenly distributed between 0 and 2π, and θ is the scattering angle. Otherwise, the medium is non-isotropic. The direction is determined by g and the Henyey-Greenstein phase functions. When the motion direction of the photon is close to vertical ($w \geq 0.9999$):

$$\begin{cases} u_{m+1} = sin\theta cos\varphi \\ v_{m+1} = sin\theta sin\varphi \\ w_{m+1} = SIGN(w) cos\theta \end{cases} \quad (3)$$

When $w > 0$, SIGN (w) = 1; w < 0, SIGN (w) = -1. Otherwise, $w < 0.9999$, the moving direction is:

$$\begin{cases} u_{m+1} = \frac{sin\theta}{\sqrt{1-w_m^2}}(u_m w_m cos\varphi - v_m sin\varphi) + u_m cos\theta \\ v_{m+1} = \frac{sin\theta}{\sqrt{1-w_m^2}}(v_m w_m cos\varphi - u_m sin\varphi) + v_m cos\theta \\ w_{m+1} = \sqrt{1-w_m^2} sin\theta cos\varphi + w_m cos\theta \end{cases} \quad (4)$$

If the weight of the photon does not drop under a certain threshold, for example 10^{-6}, the photon continues to propagate. When the weight is lower than this value, the photon's propagation only produces little information, and the photon can be considered to have died. In order to maintain energy conservation, the Russian roulette method is used to end the photon propagation. When $W < 10^{-6}$, the photon has a probability of $1/q$ (q is generally 10) to continue to propagate, and the weight is updated to qW. If the photon does not survive from roulette, its weight drops to 0.

The albedo is the ratio of all reflections to diffusive incident irradiance by the ice floe surface (Figure 1), which is acceptable during the Artic summer when overcast sky conditions are dominant (Polashenski et al., 2012). The spectral albedo α_λ, bottom transmittance $T_{b,\lambda}$, and lateral transmittance $T_{l,\lambda}$ can be calculated as the ratios of the photo weight reflected into the atmosphere, transmitted into bottom ocean, and transmitted into lateral ocean to the total weight at different wavelengths, respectively. So, the broadband albedo α, lateral transmittance T_l, and bottom transmittance T_b are as follows:

$$\alpha = \int_{\lambda_1}^{\lambda_2} \alpha_\lambda F_0(\lambda) d\lambda / \int_{\lambda_1}^{\lambda_2} F_0(\lambda) d\lambda \quad (5)$$

$$T_l = \int_{\lambda_1}^{\lambda_2} T_{l,\lambda} F_0(\lambda) d\lambda / \int_{\lambda_1}^{\lambda_2} F_0(\lambda) d\lambda \quad (6)$$

https://doi.org/10.5194/egusphere-2023-1758
Preprint. Discussion started: 8 August 2023

$$T_b = \int_{\lambda_1}^{\lambda_2} T_{b,\lambda} F_0(\lambda) d\lambda / \int_{\lambda_1}^{\lambda_2} F_0(\lambda) d\lambda \quad (7)$$

where F_0 is the incident solar irradiance. By calculating the total weight of absorbed photons in different media, we can get the energy absorbed by the pond Ψ_p, and by ice Ψ_i. It is obvious that the $\Psi_i = 1 - \alpha - T_l - T_b - \Psi_p$.

To determine the impact of limited floe and pond size on optical properties, it is necessary to examine the difference between the results of the MC model with finite medium and those calculated by linear combination α_{line}. The proportional coefficients K_α and K_T are defined as:

$$\begin{cases} K_\alpha = \alpha_{line}/\alpha \\ K_T = T_{line}/T_b \end{cases} \quad (8)$$

$$\begin{cases} \alpha_{line} = (1 - S_p/S_i)\alpha_{ice} + S_p/S_i \alpha_{pond} \\ T_{line} = (1 - S_p/S_i) T_{ice} + S_p/S_i T_{pond} \end{cases} \quad (9)$$

where the α_{ice} and α_{pond} are the bare ice and melt pond albedos with infinite horizontal scale, which can also be determined using the MC model with $d_i = \infty$, MPF = 0%, and with $d_i = \infty$, MPF = 100%, respectively. So do T_{ice} and T_{pond}.

2.3 Model parameters

The wavelength band we used in this study was 350 to 1000 nm, which covered 70 – 80 % of the solar energy reaching the Earth' surface (Liou, 2002). Incident solar irradiance under overcast sky conditions reported by Grenfell and Perovich (2008) for the month of August were selected as default settings. The absorption coefficient of pond water, which is wavelength dependent, was obtained from Segelstein (1981). The scattering coefficients of pond water and ocean were neglected (Taylor and Feltham, 2004), while the scattering coefficients of ice were 1000 m^{-1}, 70 m^{-1}, and 20 m^{-1}, corresponding to SSL, DL, and IL, respectively. The absorption coefficient of sea ice was obtained from Perovich (1996). The asymmetry parameter for pond water and sea ice were 0 and 0.94, respectively (Briegleb and Light, 2007).

3 Results

3.1 AOPs of large floe

A d_i of 2000 m was employed in this section to represent the typical Arctic floe size (Wang et al., 2020). This size was sufficiently large to ignore the impact of the horizontal scale of ice floe (see section 3.2.1 later for details), and influence of other factors are then straightforward. H_p and H_i were assumed to vary from 0 to 0.5 m and from 0.5 to 5 m. However, pond AOPs are affected not only by H_p and H_i, but also by MPF (Polashenski et al., 2012). Therefore, we also considered the influence of MPF in combination with each parameter.

https://doi.org/10.5194/egusphere-2023-1758
Preprint. Discussion started: 8 August 2023

3.1.1 Influence of H_p and H_i

H_p and H_i are the two main factors affecting the AOPs (Lu et al., 2016). Therefore, MPF was firstly assumed to be 40% for the average values of first-year ice (FYI) (Nicolaus et al., 2012). The results of AOPs are shown in Figure 2.

The broadband albedo α was influenced by both H_i and H_p (Figure 2a); specifically, it increases as H_i increases or H_p deceased. Moreover, when H_i was thinner than 3 m, the albedo was mainly controlled by this parameter. For example, as H_i increased from 1 to 3 m, the albedo increased by about 14%, while as H_p increased from 0.1 to 0.5 m, the albedo decreased only by about 0.7%. When H_i was thicker than 3 m, the albedo was less influenced by both H_p and H_i. As H_i increased from 3 to 5 m, the albedo increased by about 2%. At the same time, as H_p increased from 0.1 to 0.5 m, the albedo decreased by about 2.4%.

As shown in Figure 2b, the bottom transmittance T_b was also dependent on H_i and H_p; specifically, it was reduced as these two parameters increased. Furthermore, the response of T_b on H_i was more sensible than that on H_p. As H_i increased from 1 to 2 m, T_b decreased by 46%, while as H_p increased by 4 times (from 0.1 to 0.5 m), T_b decreased by only 17%.

The energy absorbed by pond and underlying ice were also controlled by H_i and H_p. The influence of H_p on Ψ_p is the major factor (Figure 2c). Ψ_p increases by 78% as H_p increased from 0.1 to 0.3 m, while a greater increase of H_i (from 0.5 to 5 m), caused only a 4.3% increase in Ψ_p. Ψ_i was complexed and sensitive to both H_p and H_i (Figure 2d). As the H_p increased from 0 to 0.5 m, Ψ_i decreased from 0.37 to 0.28. Meanwhile, Ψ_i increased from 0.20 to 0.36 as the H_i increased from 0.5 to 5 m.

https://doi.org/10.5194/egusphere-2023-1758
Preprint. Discussion started: 8 August 2023

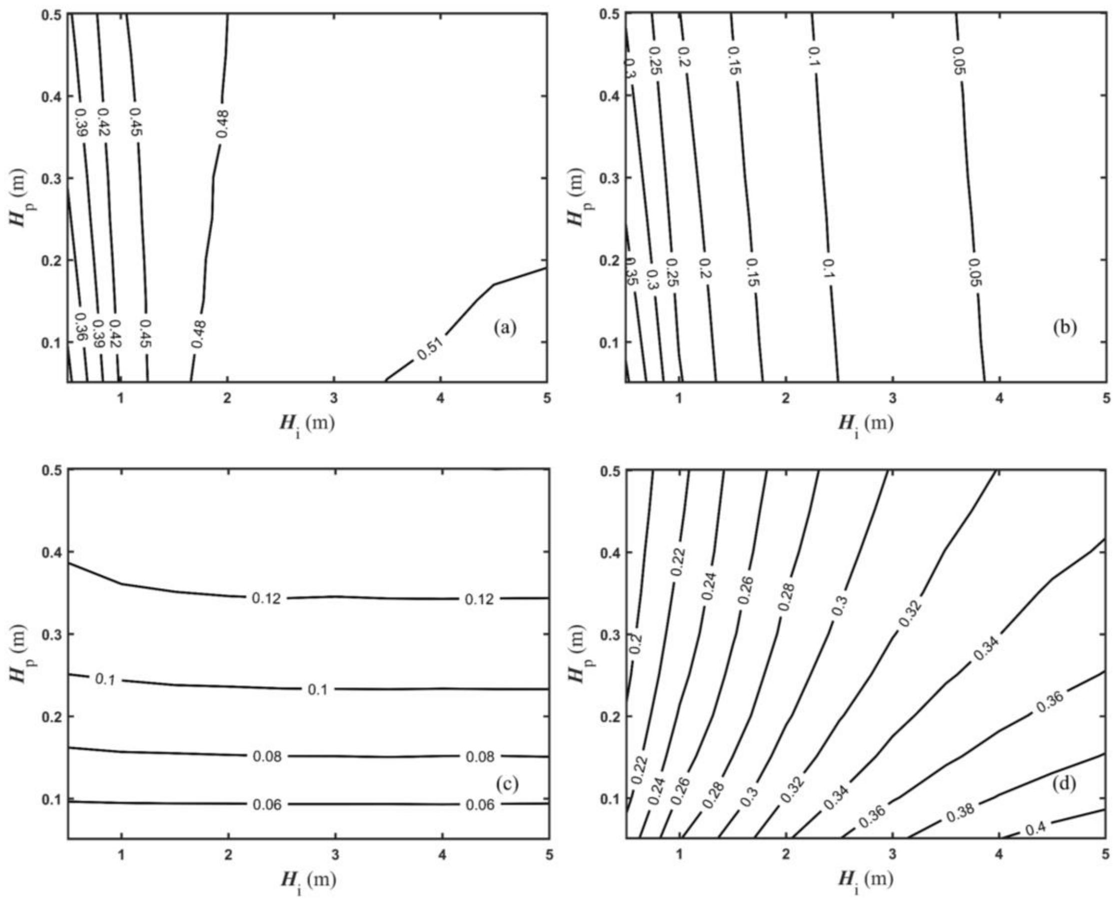

Figure 2: Variation in the portion of solar energy in relation to: (a) albedo α, (b) bottom transmittance T_b, (c) energy absorbed by the pond Ψ_p, and (d) energy absorbed by the underlying ice Ψ_i.

3.1.2 Influence of MPF and H_i

A constant pond depth of 0.25 m was set to highlight the impact of both MPF and H_i. Figure 3a shows that the albedo is decided by both MPF and H_i for thin ice (H_i < 1.5 m), and mainly determined by MPF for thick ice (H_i > 1.5 m). For the thin ice, the albedo increased from 0.37 to 0.49 as H_i increased from 0.5 to 1.5 m with MPF = 36%. At the same time, the albedo decreased from 0.59 to 0.21 as MPF increased from 0 to 100% with H_i = 1 m. For thick ice, the albedo increased only slightly from 0.50 to 0.52 as H_i increased from 2 to 5 m with MPF = 36%. However, the average albedo of thick ice decreased from 0.65 to 0.28 (by about 57%) as MPF increased from 0 to 100%.

T_b was shown to be controlled by both H_i and MPF (Figure 3b). Firstly, T_b decreased as H_i increased, which was consistent to the results shown in Figure 2b. The average T_b at different MPFs decreased from 0.33 to 0.03 as H_i increased from 0.5 to 5 m. Secondly, it was observed that if H_i and H_p did not vary, the lateral sea ice areas of the pond decreased with the increase

https://doi.org/10.5194/egusphere-2023-1758
Preprint. Discussion started: 8 August 2023

of MPF, leading to a decrease in the total ice floe areas, which in turn increased the transmittance. For example, the average T_b at different H_i values increased from 0.08 to 0.18 as MPF increased from 0 to 100%.

Figure 3c shows that Ψ_p was mainly counted on MPF. As the MPF increased from 0 to 1, Ψ_p increased from 0 to 0.26, while as H_i increased, the Ψ_p at different MPFs remained almost constant. Ψ_i was mainly related to H_i and less to MPF (Figure 3d). The average Ψ_i at different MPFs increased from 0.20 to 0.36 as H_i increased from 0.5 to 5 m, while the average Ψ_i at different H_i values increased from 0.30 to 0.31 as MPF increased from 0 to 100%.

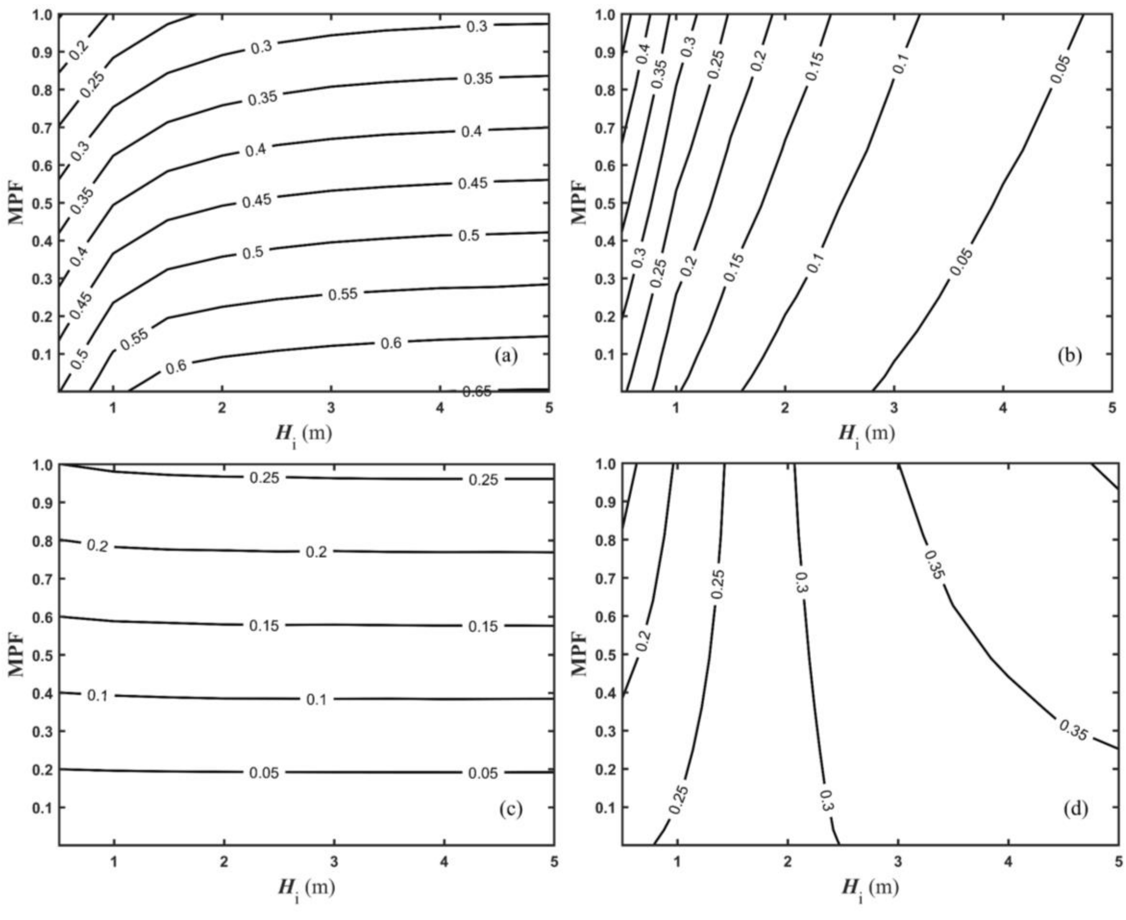

Figure 3: Variation in the portion of solar energy in relation to: (a) albedo α, (b) bottom transmittance T_b, (c) energy absorbed by the pond Ψ_p and (d) energy absorbed by the ice Ψ_i at H_p = 0.25 m.

3.1.3 Influence of MPF and H_p

A constant underlying ice thickness of 2.5 m was assumed to investigate the effect of MPF and H_p. The results showed that the albedo depended more on MPF than on H_p (Figure 4a). It decreased from 0.64 to 0.27 (by 58%) as MPF increased from 0

https://doi.org/10.5194/egusphere-2023-1758
Preprint. Discussion started: 8 August 2023

to 100%, while it decreased only slightly as H_p increased. For example, the albedo decreased from 0.51 to 0.50 with MPF = 36% as H_p increased from 0.05 to 0.5 m. T_b was also mainly dependent on MPF (Figure 4b), which increased from 0.06 to 0.14 as MPF increasing from 0 to 100%.

Ψ_p depended on both H_p and MPF (Figure 4c). Further, with the increasing of H_p, Ψ_p began to rely mainly on H_p and MPF (H_p < 0.15 m), and finally mainly depended on MPF. At H_p < 0.15 m, Ψ_p increased from 0 to 0.2 as H_p and MPF increased to 0.15 and 100%, respectively. At H_p > 0.15 m, the average Ψ_p increased from 0 to 0.25 as MPF increased from 0 to 100%. While as H_p increased from 0.15 to 0.5 m, Ψ_p increased from 0.20 to 0.35 with MPF = 100%, which shows the influence of H_p is some smaller than that of MPF. Ψ_i was connected to MPF and H_p (Figure 4d). The average Ψ_i at different H_p values increased from 0.3 to 0.33 as MPF increased from 0 to 100%. As H_p increased from 0 to 0.5 m, the average Ψ_i decreased from 0.35 to 0.29.

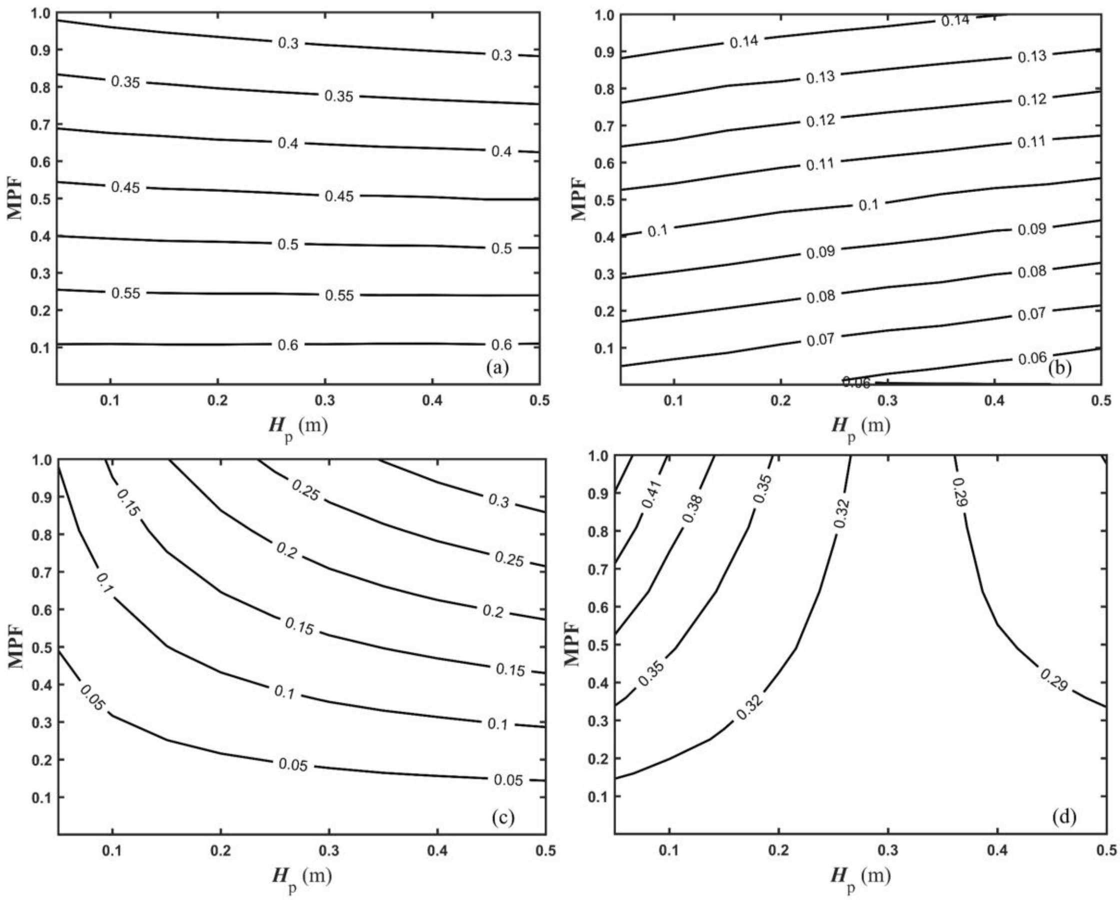

Figure 4: Variation in the portion of solar energy in relation to: (a) albedo α, (b) bottom transmittance T_b, (c) energy absorbed by the pond Ψ_p and (d) energy absorbed by the ice Ψ_i at the H_i = 2.5 m.

https://doi.org/10.5194/egusphere-2023-1758
Preprint. Discussion started: 8 August 2023

3.2 AOPs of small floes

Incident solar radiation can be transmitted not only to the ice bottom, but also to the lateral side of sea ice (Petrich et al., 2012). In contrast to the above results obtained for large floes, the lateral transmittance T_l of small floes cannot be ignored, as it can have important effects on other AOPs. Such as the T_b and albedo, which increase with increasing ice floe size (Light et al., 2003). To estimate T_l and investigate its impact on the AOPs of ice floes with limited horizontal scale, H_p = 0.3 m and H_i = 1.0 m were used in the simulation, which are the typical values for ponds on FYI (Perovich et al., 2009). The results are reported in the subsections below.

3.2.1 The influence of floe size on AOPs

Two limit cases, MPF = 100% and 0% with different d_i were considered to explore the influence of the horizontal extent of different media (pond and sea ice).

Figure 5 shows that with the increase in pond or ice floe size, T_l gradually decreased while the other AOPs increased. For small-size floe, the T_l at MPF = 100% was larger than that at MPF = 0%. T_l decreased from 0.42 and 0.24 to almost 0 as floe size increased from 2 to 200 m, respectively, at MPF = 100% and 0%. When the melt pond or ice floe sizes reached 200 m, the AOPs were nearly constant, i.e., T_l did not affect the other pond and ice AOPs. At the same time, as floe size reached 200 m, the AOPs were almost consistent with those at $d_i = \infty$. Figure 5 also shows that the influence of T_l on the other AOPs was less than 5% when floe size reached 40 m, regardless of whether MPF = 100% or 0% (red points in the figure), specifically, T_l was 2.9% and 1.6%, respectively.

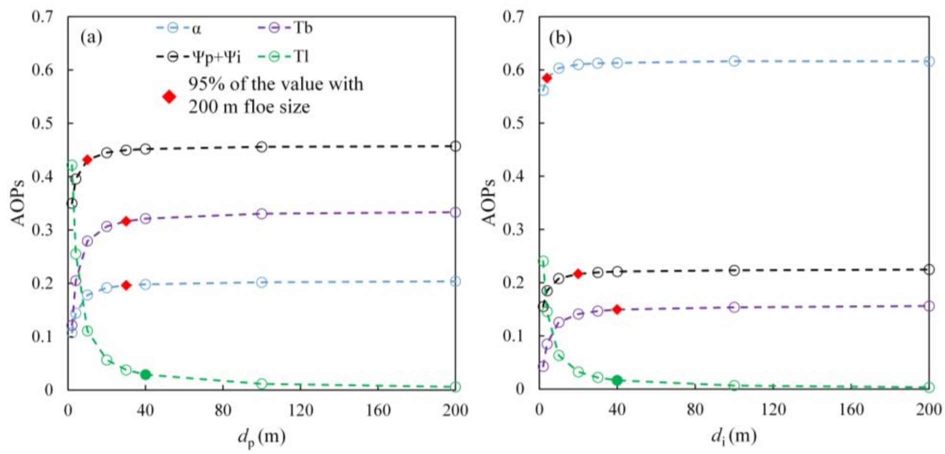

Figure 5: Variation of AOPs with (a) pond size with MPF = 100% and (b) ice size with MPF = 0%.

https://doi.org/10.5194/egusphere-2023-1758
Preprint. Discussion started: 8 August 2023

3.2.2 Accuracy of the linear combination method

The variation of both K_α and K_T can be determined based on Eq. (8). Figure 6 shows that these two parameters were closely related to floe size and MPF. As floe size increased from 2 to 200 m, K_α and K_T decreased from 2 to 1.02 and from 3.08 to 1.02, respectively, at MPF = 100%. The losses of solar radiation at the sidewalls are known to cause large differences between the AOPs of small and large ice floe. An increase in the horizontal size can make the floe behave more like that of the horizontal infinite medium (Light et al., 2003).

K_α increased as MPF increased (Figure 6a), and the peak was detected at MPF = 100% under the same floe size. For example, K_α increased from 1.1 to 2 for floe with a size of 2 m as MPF increased from 0 to 100%. This can be due to the fact that pond water only absorbs solar radiation while sea ice absorbs and scatters it (Taylor and Feltham, 2004). As MPF increased, the scattering decreased and more photons interacted directly with the sidewalls (Figure 5), causing greater sidewall losses and an increase in K_α for specific floe size. Furthermore, the smaller the floe size, the greater the dependence of K_α on MPF. For example, as MPF increased from 0 to 100%, K_α increased by 80% for 2-m floe, and by 4% for 40-m floe.

Unlike K_α, K_T decreased as MPF increased (Figure 6b). However, except in the case of small-sized floe size (2 m), K_T decreased little as MPF increased. Specifically, as MPF increased from 0 to 100%, K_T decreased by 10.1% and 0.7% for floe with sizes of 6 and 40 m, respectively. Due to the influence of T_l on small-sized floe (Figure 5), the K_T of the 2-m floe decreased from 4.7 to 3.1, by about 34%. However, the absolute difference between T_{line} and T_b increased with the increase of MPF, and the reason is similar to that proposed for K_α. The decrease of K_T was mainly due to the relatively small T_b values (Figure 5).

For relatively small ice floe (d_i < 20 m), T_l must be considered when measuring the albedo and T_b, especially for in suit measurements of UAVs (Figure 6). For large-sized floe (200 m), K_α and K_T were shown to be almost 1. These results provide a theoretical basis for using satellite remote sensing to calculate the albedo of Arctic floe surfaces with a large horizontal extent.

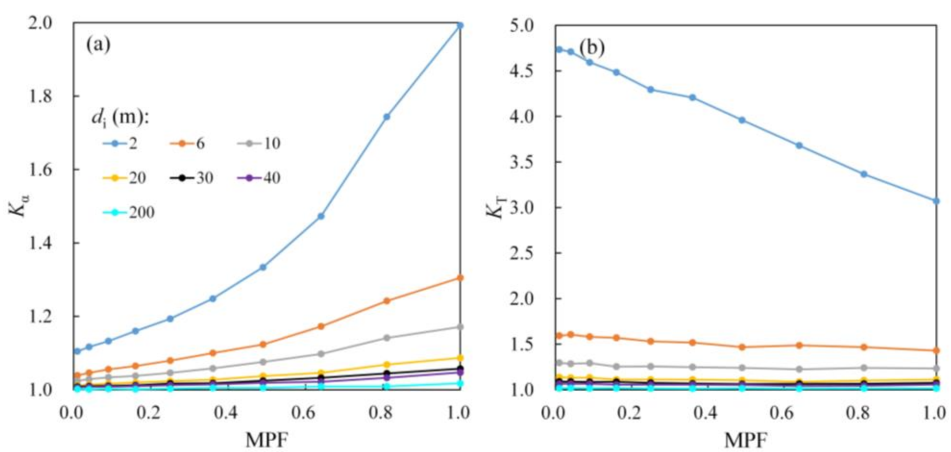

Figure 6: Proportional coefficient of (a) albedo K_α and (b) bottom transmittance K_T calculated via the MC model and linear combination.

3.3 Vertical distribution of solar radiation in ponded ice floe

The MC model was used to calculate the distribution of net irradiance F_{net} for different MPFs and floe sizes and thus explore the allocation of solar radiance absorbed by sea ice and the ocean (Figure 7). The rate of energy absorbed per unit volume (i_e) was also found to be significant for the ice floe. This parameter is an important source term in the heat conduction equation. It illustrates the contribution of solar irradiance heating to the warming and melting in sea ice. Taylor and Feltham (2004) described the energy absorption rate are follows:

$$i_e = -\int_{\lambda_1}^{\lambda_2} \frac{\partial F_{net}(z,\lambda)}{\partial d} d\lambda \tag{10}$$

Three different melt pond types were assumed in this study:
Case I: an open pond with a floe size of 2 m and MPF 40%.
Case II: an open pond with a floe size of 2000 m and MPF 40%.
Case III: an open pond with a floe size of 2000 m and MPF 10%.
Case I and II were used to emphasize the influence of floe size, while case II and III to highlight the impact of MPF. The incident spectral irradiance Q_{sw} was 164.5 W/m^2. The net irradiance distribution in the floe system for the three cases is shown in Figure 7a – c, and the energy absorption rate is shown in Figure 7d.
Most of the incident irradiance was dissipated in the pond and surrounding sea ice (Figure 7a – c). The solar radiance absorbed by the floe was mainly in the NIR band. The irradiance penetrating the ocean was mainly between 350 and 750 nm. The energy in the band of 750 – 1000 was completely absorbed in the floe, especially those ranging from 900 to 1000 nm, which had the largest absorption for ice and pond water compared to the other bands. Due to the existence of the SSL on the ice surface, the albedo of the floe (0.38 – 0.58) was larger than that of melt pond (0.15 – 0.34) and the transmittance (0.14 – 0.22) is smaller than that of pure pond (0.20 – 0.39) (Hudson et al., 2013).
The variation of MPF and floe size did not affect the relative magnitude of i_e (Figure 7d). Overall, i_e was large at the floe surface and d/30. It dropped significantly in the range of 0 to 0.3 m and then continue to gradually decrease of the remaining radiation. Sudden variations in i_e were then observed at d/30 and 0.3 m. The first change in i_e was mainly related to the SSL of ice. On the one hand, the radiation in the NIR band was rapidly by pond water and ice. On the other hand, the SSL reflected most of the solar radiation. The second change in i_e was mainly attributed to the different inherent optical properties (IOPs) of the two media, especially for pond water and sea ice. However, the smaller changes observed in case III at d/30 were due to the small MPF (only 10%).
When Comparing cases I and II, where MPF was the same, the largest difference in irradiance distribution between small and large-sized floe was detected in the 450 – 550 nm band (Figure 7a and b). The smaller the floe size, the easier it was for solar radiation to penetrate the lateral ocean (Figure 6). The net irradiance was lower in case I than in case II, especially in the above-mentioned band. The net irradiance peaks at the ice bottom in cases I and II were 0.098 W/m^{2}nm, and 0.16

https://doi.org/10.5194/egusphere-2023-1758
Preprint. Discussion started: 8 August 2023

W/m^{2}nm, respectively, and both of them were in the 480 nm. At the same time, the i_e on the ice surface decreased from 83.2 to 37.9 w/m^3 as floe size increased from 2 to 2000 m (Figure 7d).

MPF also had a major impact on the distribution of radiation through the sea ice (Figure 7b and c). The results obtained for net irradiance suggested that the SSL worked as an interlayer and prevented much of the solar radiation from reaching the floe system. The peak net irradiance at the ice bottom in case III was 0.12 W/m^{2}nm in the 460 nm, which was smaller than that of case II. The i_e on the floe surface increased from 21.3 to 37.9 w/m^3 as MPF increased from 10% to 40%, which corresponded to an increase of 78% (Figure 7d). This increase remained about 32% in floe depth of 0.4 – 1.3 m. This situation was reasonable. Because as MPF increased, the solar radiation directly absorbed by the pond also increased, resulting in the increase of i_e. The sudden change in i_e at d/30 was also affected by MPF. For example, at MPF =10%, i_e increased from 11.6 to 38.6 w/m^3, which corresponded to a 233% increase, while at MPF = 40%, it increased from 24.0 to 39.9 w/m^3, i.e., only by about 66%.

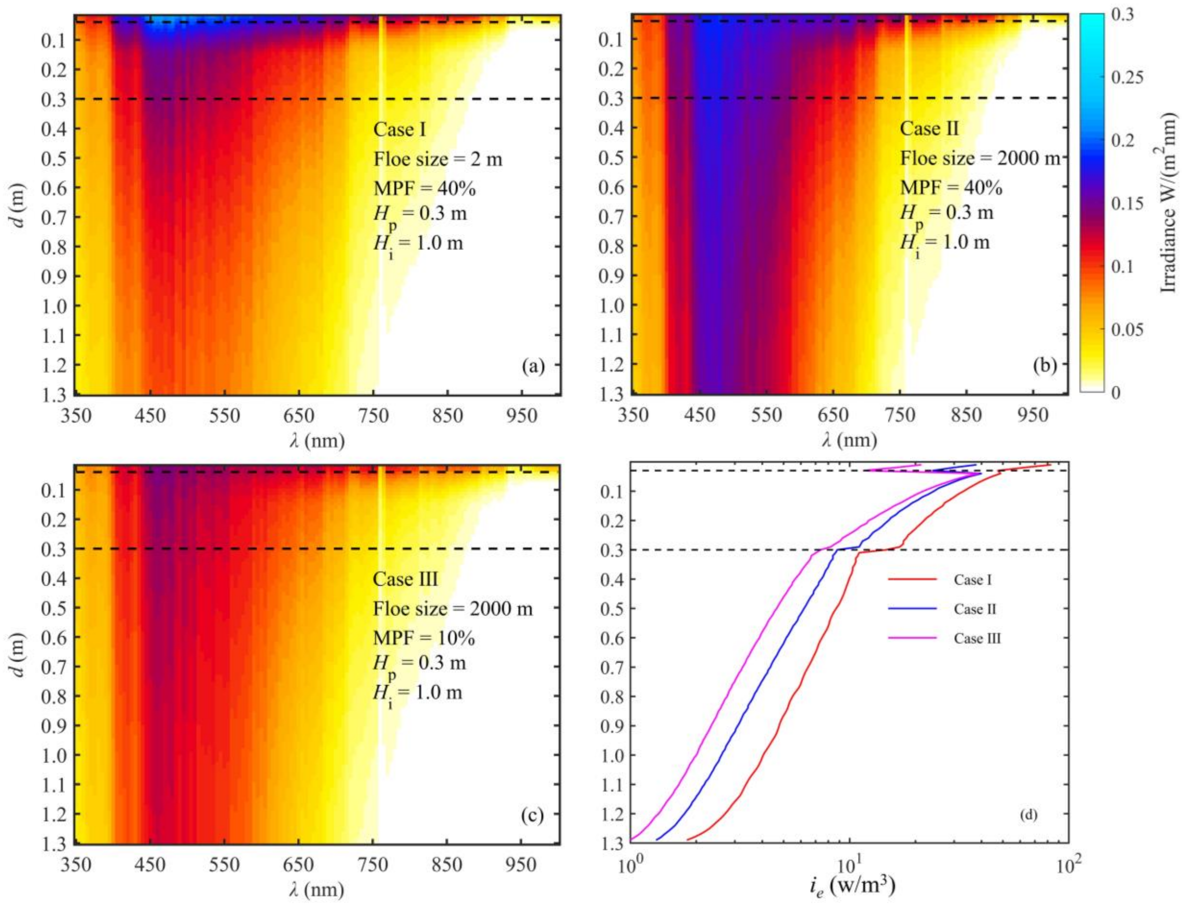

Figure 7: Distribution of spectral net irradiance F_{net} in the floe system under three different cases: (a) Case I, floe size = 2 m and MPF = 40%, (b) Case II, floe size = 2000 m and MPF = 40%, and (c) Case III, floe size = 2000 m and MPF = 10%. The dashed line represents the SSL and pond depth. The variation in the energy absorption rate i_e by the ice floe in the three cases is shown in (d).

https://doi.org/10.5194/egusphere-2023-1758
Preprint. Discussion started: 8 August 2023

4 Discussion

4.1 Comparisons and validations

4.1.1 Comparisons with numerical simulations

The delta-Eddington model (Briegleb and Light, 2007, BL model hereafter) can calculate the AOPs of melt pond with plane-parallel, infinite horizontal case. The albedo and T_b were verified as functions of H_p, g, and H_i = 1.0 m corresponding to FYI (Figure 8) and were calculated for pond depths ranging from 0.1 to 0.5 m and g values for underlying sea ice of 0.88, 0.90, 0.92, 0.94, and 0.96. The MC and BL models produced similar results, and a small relative difference (less than 3%) between models was observed under different g and H_p.

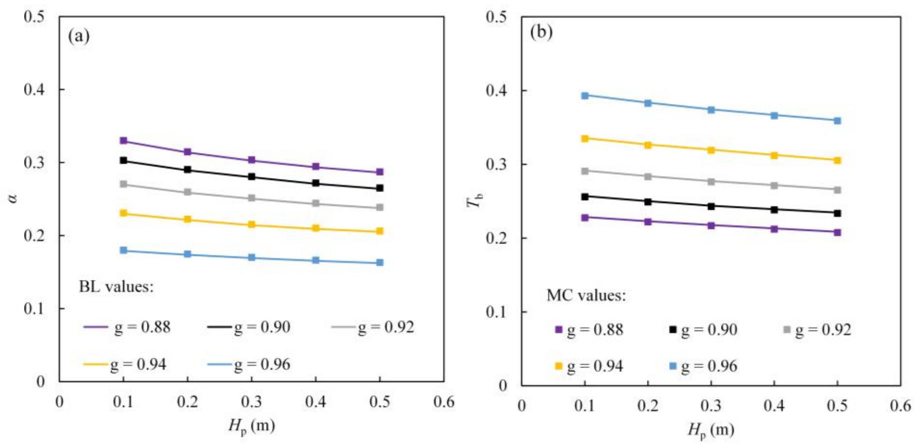

Figure 8: Comparison of (a) albedo and (b) T_b as functions of pond depth and asymmetry parameter estimated by the MC and BL models. The underlying ice thickness was 1.0 m.

Zege et al. (2015) (Zege15 hereafter) estimated the spectral albedo of the ice floe with different MPF. Figure 9 shows the comparison between the Zege15 and present MC model. There were two cases: For case I, MPF, optical properties of pond water, optical thickness of ice beneath of pond, effective optical thickness of white scattering layer of the surrounding ice were 0.4, 0.016, 3.0, and 8.5, respectively. Corresponding parameters of case II were 0.24, 0.007, 0.93, and 5, respectively. All characteristics were given at wavelength of 550 nm. The above-mentioned parameters were input into MC model to estimate pond AOPs. The R^2 between the simulated by the MC model and Zege15 was higher than 0.97, with $P < 0.01$, and the $<\zeta>$ was within 4%. The maximum difference in spectral albedo between the models was less than 0.05. The root mean square error ε was also within 0.02.

https://doi.org/10.5194/egusphere-2023-1758
Preprint. Discussion started: 8 August 2023

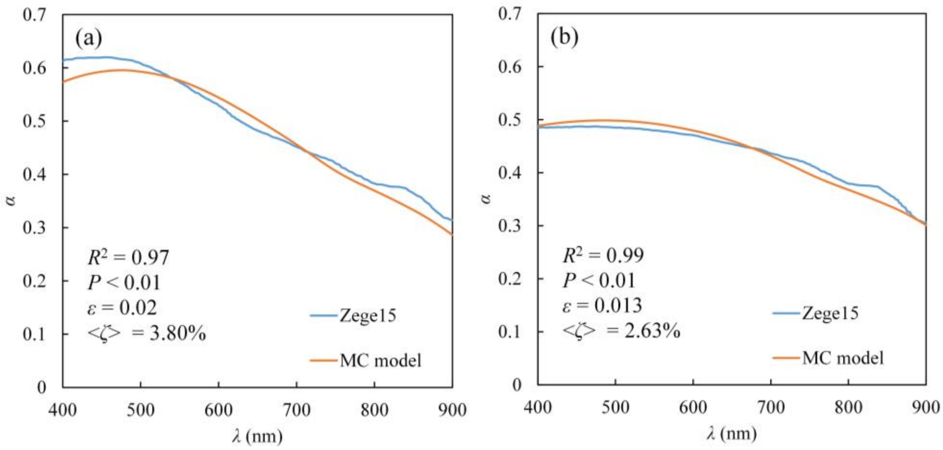

Figure 9: Comparison of the simulated spectral albedo between Zege15 and the MC model: (a) case I with MPF = 0.4, and (b) case II with MPF = 0.24.

Light et al. (2003) (Light03, hereafter) estimated K_T of a cylindrical sea ice samples by using a two-dimensional Monte Carlo radiative transfer model. The incident irradiance was collimated and normal to the top of the sample. The scattering of the medium was assumed isotropic. The thickness of the cylinder was 50 cm. The optical depth ranged between 7 and 8, then K_T depended mainly on the cylinder radius. The refractive index was 1.3, and g = 0. As the cylinder radius increased from 0.25 to 1.07 m, the K_T of Light03 decreased from 3.33 to 1.05. Figure 10 shows the comparison of the estimated results of Light03 and the present model. The R^2 in both our simulation and Light03 was 0.93, with $P < 0.07$, the ε = 0.38 and the <ζ> = 12%. The differences in K_T of 0.25 m cylindrical sample were larger than that of the other sample. This can be attributed to the fact that in cylinders with a smaller radius, more photons are absorbed by the sidewalls, causing the detector at the ice bottom to receive only a few photons.

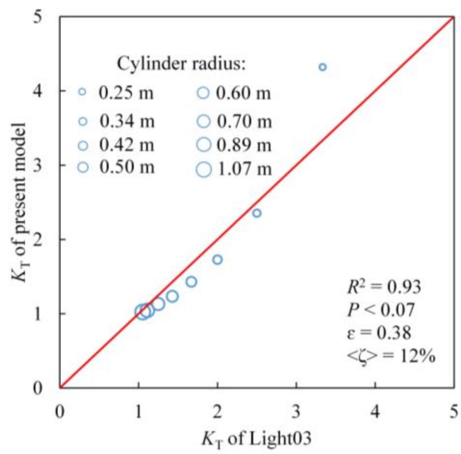

Figure 10: Comparison between K_T values simulated in by Light et al. (2003) and our MC model.

https://doi.org/10.5194/egusphere-2023-1758
Preprint. Discussion started: 8 August 2023

4.1.2 Comparisons with experimental results

Zhang et al. (2023) conducted "artificial pond" experiments with different pond sizes on Hanzhang Lake in the winter of 2022. The artificial pond had a hexagonal edge and a fairly flat bottom. The total ice thickness was 0.4 m (d = 0.4 m). H_p was set to 0.05, 0.10, 0.15, 0.20, and 0.25 m, which corresponded respectively to H_i values of 0.35, 0.30, 0.25, 0.20, and 0.15 m. The inherent optical properties of the lake ice are different from those of Arctic sea ice. The scattering coefficient of lake ice was mainly determined by gas bubbles, and was determined according to Grenfell (1991) and Yu et al. (2022). The values of g range from 0.851 to 0.865, with an average of 0.860 (Malinka et al. 2018). Once g and the scattering coefficient of the ice have been determined, the absorption coefficient can be inferred using the radiative transfer model (Light et al., 2003).

These IOPs were implemented in the MC model, and the simulated α, Ψ_p, and Ψ_i were compared with the AOP measurements, as shown in Figure 11. The correlation coefficient R^2 are higher than 0.95 with statistic significant ($P < 0.01$). The root mean square error for AOPs was relatively small and the maximum average relative error <ζ> was 7.4% for Ψ_i. This demonstrated the reasonable of the MC model with finite medium. However, the correlation between the simulated and measured T_b was not well enough (Figure 11b). It attributed to the narrow range of measured T_b under a nearly constant ice thickness.

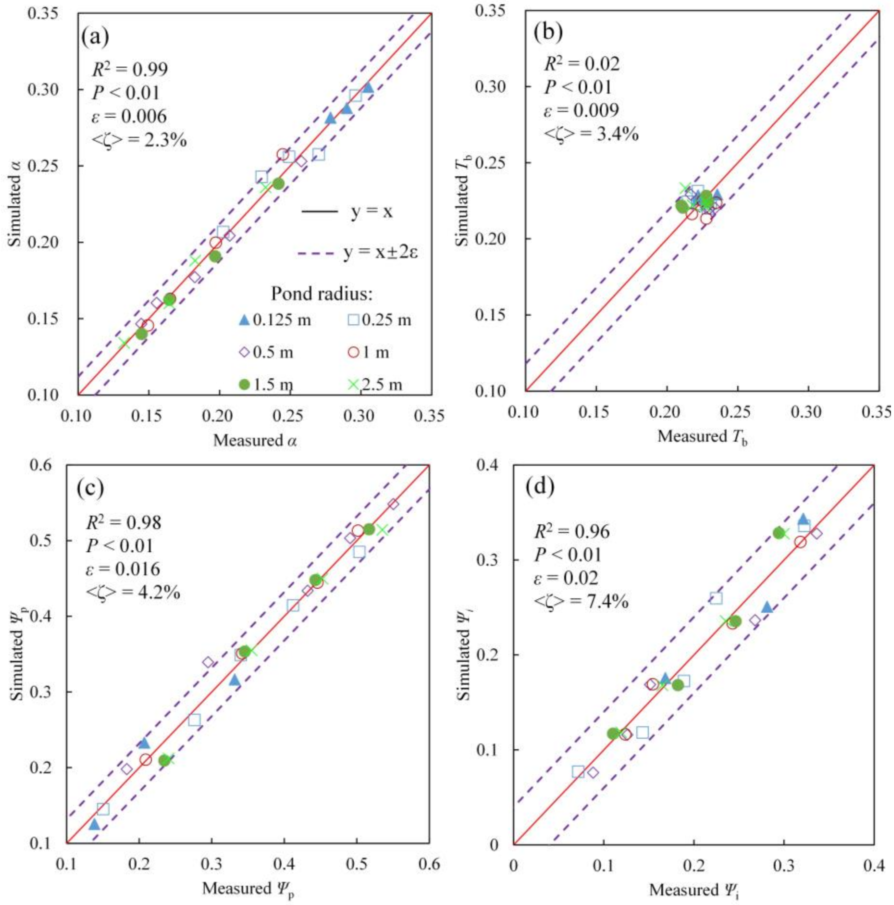

Figure 11: Comparison between the measured and simulated AOPs for the finite pond size: (a) albedo, (b) bottom transmittance, (c) energy absorbed by pond, and (d) energy absorbed by ice.

4.1.3 Comparisons with in situ measurements

The in-situ measurements of melt pond evolution by Polashenski et al. (2012) provide a nice validation of our MC model. The floe thickness decreased from 1.2 m to 0.95 m as the melting of sea ice. And the average pond depth along the 200 m line increased from 0 to 0.25 m. The measurements were conducted on seasonal landfast Arctic sea ice. Floe size was then set to 2000 m in the MC model to avoid the lateral transmittance (Figure 5). Three different stages were examined, i.e., pond formation, pond drainage and pond evolution, which are referred to as stages I, II, and III, respectively (Figure 12).

The simulated albedo with the MC model agrees with the observed results with R^2 = 0.88, the P < 0.01, ε = 0.035 and the $<\zeta>$ is 6.6% (Figure 12). On the fifth day since the beginning of pond formation, MPF was the largest (0.5). However, the measured albedo was larger than on the fourth day. This may be due to the snowfall. Furthermore, the simulated albedos were larger than the measured values in stage I, because the melting of the sea ice surface caused the overlying snow to melt

https://doi.org/10.5194/egusphere-2023-1758
Preprint. Discussion started: 8 August 2023

as well. This would generate wet snow and black ice, which would significantly decrease the scattering coefficient of sea ice (Polashenski et al., 2012). In stage II, melt pond drainage increased the roughness of the ice surface and reduced pond coverage, potentially leading to a very high ice permeability and consequence increase in the scattering coefficient of sea ice (Polashenski et al., 2012). As a result, the albedo of ice on the 11th day with an MPF of 8.3% was larger than that of pure ice. At stage III, MPF increased and albedo slightly decreased.

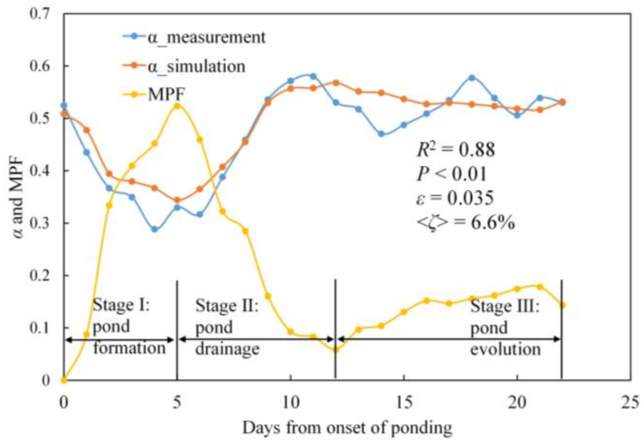

Figure 12: Simulated albedo, measured albedo, and MPF versus days since the onset of pond formation.

4.2 Variations in K_α and K_T with Arctic latitude

Arctic floe size always increases with latitude (Xie et al., 2013), further affecting the AOPs of sea ice according to Figure 5. The floe and melt pond observed obtain during the 5th Chinese National Arctic Research Expedition (CHINARE) on the icebreaker R/V *Xuelong* in the summer of 2010 were used here to quantitatively estimate the effects of floe size at different latitudes on AOPs in the real Arctic environment (Xie et al., 2013). The ship-based measurements at different latitudes were divided into two groups based on time collection, i.e., during the northward or southward legs. The northward leg started at 71.35°N, 156.94 °W on July 25, and ended at 88.36°N, 177.52 °W on August 25. The southward leg started on August 20 and ended on August 28. The northward leg was divided into three sections: marginal ice zone (ice concentration < 60%) (71°N – 75°N), part of the ice concentration < 60% (75°N – 77.5°N), ice concentration > 60% (> 77.5°N). The southward leg was divided into two sections: marginal ice zone (75°N – 80°N) and others (ice concentration > 60%) (> 80°N). The average ice thicknesses and MPFs recorded at different latitudes are shown in Figure 13a, and b. To calculate the maximum T_l of floe at these latitudes, the lower limit of the floe size code with latitude is shown in Figure 13c. Pond depth was assumed to be 0.1 m based on the average pond depth in typical FYI reported in Polashenski et al. (2012).

https://doi.org/10.5194/egusphere-2023-1758
Preprint. Discussion started: 8 August 2023

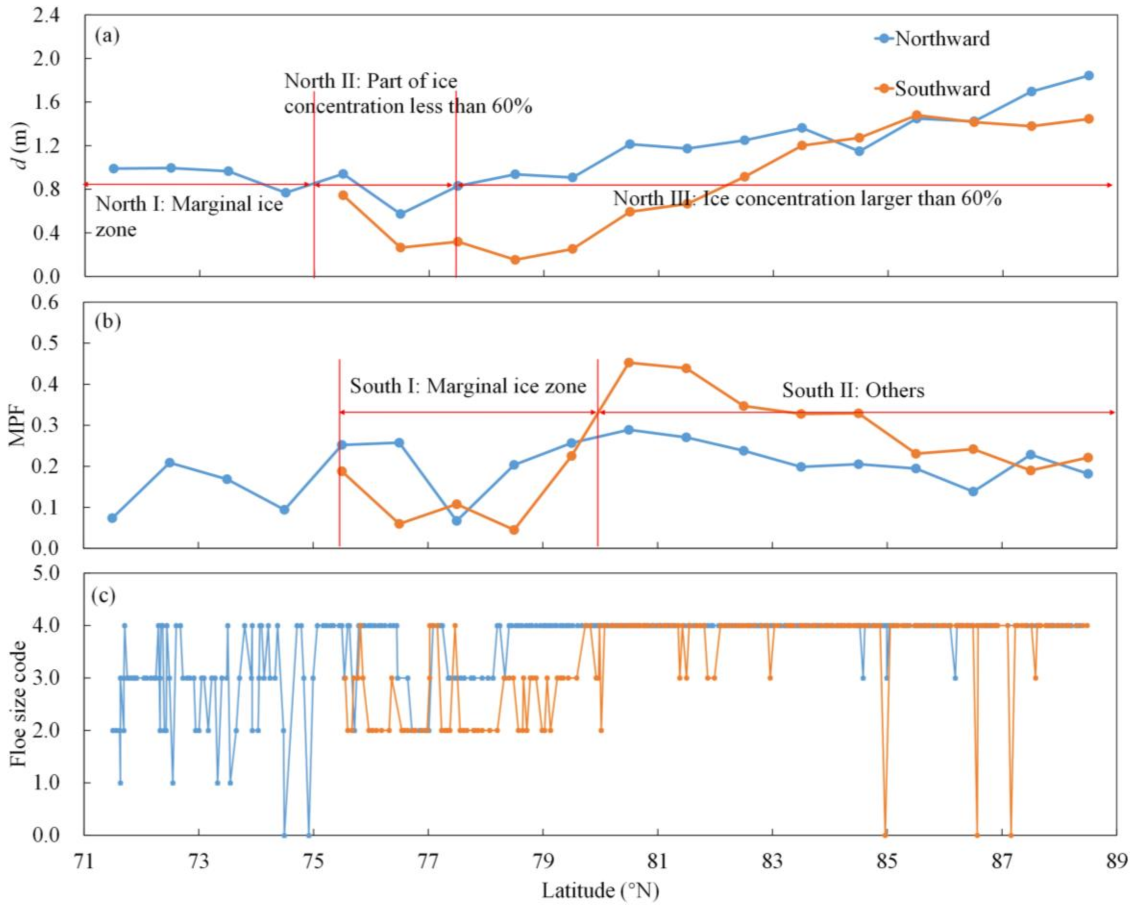

Figure 13: Ship-based observations of (a) sea ice thickness, (b) MPF, (c) floe size code during the CHINARE-2010, from July 25 to August 20 (northward leg), and from August 20 to 28 (southward leg). Floe size codes: 1 (1 m), 2 (2 m), 3 (20 m), and 4 (100 m). The northward and southward legs are indicated by the blue and yellow lines, respectively.

Figure 14 shows the T_l along the cruise track calculated using the observed ice thickness, size, and MPF. It is clear that T_l was almost to zero at latitude larger than 80°N, because the relatively larger floe size (100 m) in this zone prevented solar irradiance from penetrating the lateral ocean (Figure 5). Maximum T_l was larger during the northward leg (0.38) than during the southward leg (0.24). This is because small-sized floe ice was presented in 71 – 74°N (< 2 m).

Because ice was thicker in the zone covered during the northward leg, the variation of T_l for the same floe code was relatively small (Figure 14a). When ice floe size was 1 m, T_l was the largest (about 0.38); when it was 2 m, T_l varied from 0.23 to 0.27 depending on ice thickness; when it was 20 m, T_l was approximately 0.03. During the southward leg of floe code 2 m, when the ice floe was thicker than 59 cm, T_l was 0.24. As it decreased to 15 cm, T_l decreased from 0.24 to 0.08.

The average K_α and K_T decreased with increasing latitude (Figure 14b and c). In both legs, the marginal ice zone was shown to have the largest influence on K_α and K_T. During the northward leg, K_α and K_T were about 1.03 and 1.16, respectively; and

https://doi.org/10.5194/egusphere-2023-1758
Preprint. Discussion started: 8 August 2023

they were 1.03, and 1.08 for the southward. In north II, due to the presence of an ice concentration of less than 60% and small-sized floe (2 m), the influence of lateral transmittance decreased. And the values of K_α and K_T were also smaller compared to those in north I (1.02 and 1.05). In north III and the latitude larger than 80°N of the southward leg, lateral transmittance can be negligible, and K_α and K_T are almost to 1.0.

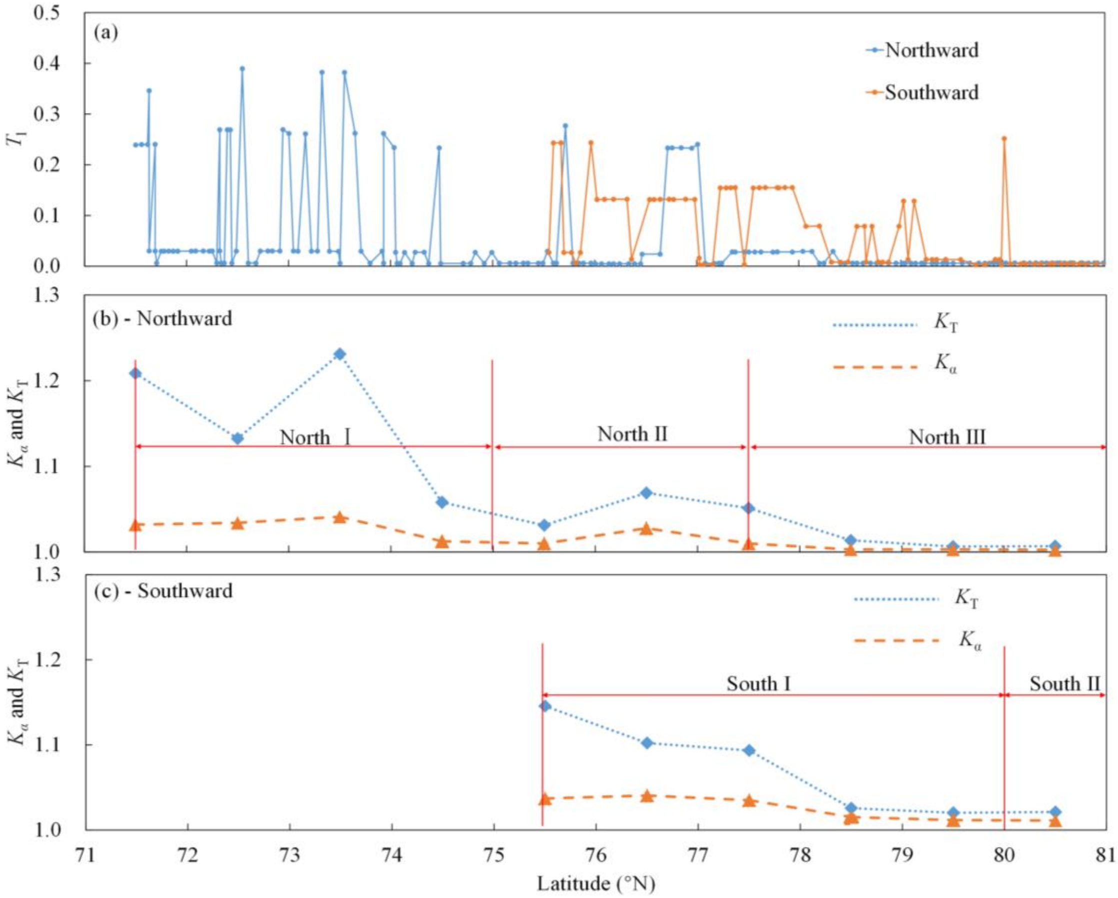

Figure 14: (a) T_l of ice floe of northward leg and southward leg for different latitudes, the corresponding K_α and K_T for different latitude of (b) northward leg and (c) southward leg.

Figure 15 shows the parameterization schemes for both K_α and K_T (including an explicit description of floe size) for the marginal ice zones, where the impact of small-sized floe on the surface albedo cannot be ignored. The general formula is K = A × lat + B, where A and B are empirical constants determined by curve fitting. The correlation coefficients $R^2 > 0.56$ and $P < 0.07$. It should be noted that the different parameterization between northward and southward legs was due to the different months during which the expedition took place. K_α decreased from 1.03 and 1.04 to 1.01, while K_T decreases from 1.21 and 1.15 to 1.03 and 1.02 during the northward and southward legs, respectively. Due to the southward cruise was conducted in late August, which contained abundant small floes (Figure 13c), the latitude of marginal ice zone for southward is larger than

https://doi.org/10.5194/egusphere-2023-1758
Preprint. Discussion started: 8 August 2023

the northward. Furthermore, during the northward leg, the floe size codes in the marginal ice zones caried from 1 to 4, while during the southward leg, they varied less, only between 2 and 3. This contributes the correlation coefficients of the parameterization results for southward leg are larger than the northward leg. During the southward leg, floe ice was thinner and K_T was smaller. This is because with thinner ice, fewer photons reached the floe boundary and then penetrated to the ocean (Light et al., 2003).

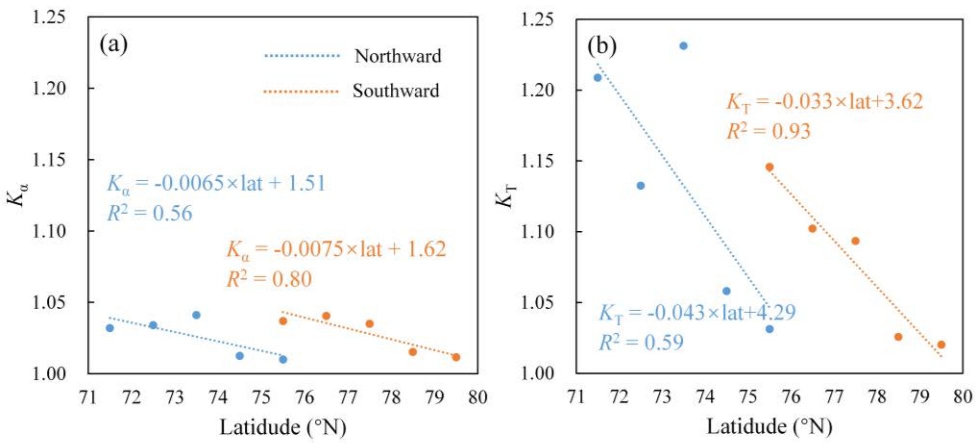

Figure 15: Variation of (a) K_α and (b) K_T with latitude for the northward and southward legs.

4.3 Variations in K_α and K_T with pond evolution

Both floe size and MPF were shown to affect the AOPs, and the latter always varied obviously during pond evolution (Figure 12). The floe size observed by Xie et al. (2013) mainly varied from 2 to 20 m for the westward leg in the marginal ice zones, which was started at -166°W to -158°W, near 71.35°N, but the pond evolution could not be measured directly on these small floes. Therefore, we have to use variations in H_p, H_i, and MPF with pond evolution in Polashenski et al. (2012). This was acceptable because firstly the above two in-situ measurements were conducted in very close locations and date. And secondly, previous observations did not reveal obvious differences in pond evolution on sea ice with small or large horizontal size (e.g., Perovich et al., 2002; Perovich and Polashenski, 2012; Polashenski et al., 2012; and Webster et al., 2022). As a result, it was possible to determine the variation of K_α and K_T during pond evolution by combining the above observations, as shown on Figure 16.

The variation of K_α and K_T was shown to be complex. On the one hand, K_α and K_T increased as floe size decreased. This is because the floe size can significantly affect the lateral transmittance (Figure 5). The smaller the floe size, the larger T_l is. On the other hand, K_α increased as MPF increased, while the K_T increased as H_i decreased. This is owing to that the albedo was mainly determined by MPF (Figure 3a). T_b was mainly determined by H_i (Figure 3b). For thin ice floe, the scattering is small

https://doi.org/10.5194/egusphere-2023-1758
Preprint. Discussion started: 8 August 2023

and only a few photons reach the sidewalls. But as ice thickness increases, so does the scattering and more photons can reach the sidewalls, causing larger sidewall losses (Light et al., 2003). Therefore, we determined the formulas to calculate K_α and K_T during different stages of pond formation: $K_\alpha = 1.01 + 1.35 \times \text{MPF} \times d_i^{-1.07}$, $R^2 = 0.89$, and $P < 0.05$ (Figure 16a); and $K_T = 1.02 + 6.63 \times H_i \times 236.6 \times d_i^{-1.63}$, $R^2 = 0.95$, and $P < 0.05$ (Figure 16b). The d_i varied between 2 and 20 m. As floe size increased, K_α and K_T converged to almost 1.0. The maximum MPF was 50% and sea ice thickness was thinner than 1.4 m, which corresponded to the typical FYI (Zhang et al., 2018; Polashenski et al., 2012).

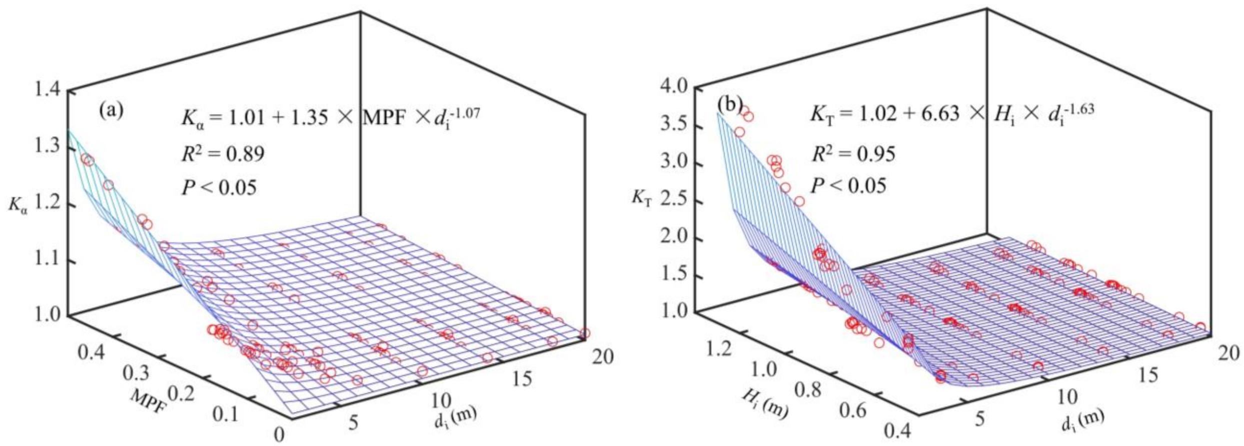

Figure 16: Variation of (a) K_α with floe size and MPF, and (b) K_T with floe size and H_i.

4.4 Recommendations for melt pond retrievals

Based on the above results, the infinite parallel plane assumption is only reasonable for quite large melt pond. According to Figure 5a, when the floe size reaches 40 m, the lateral transmittance is relatively small and can be ignored ($T_l = 0.029$) for the limit of MPF = 100%. That is to say, difference between albedo of a 40 m-pond and infinite parallel plane is less than 5% (Figure 5a). Therefore, we can regard the melt pond as horizontally infinite as its size greater than 40 m.

Things are different for a small size floe. The linear combination method can clearly overestimate the albedo and bottom transmittance especially when the floe size is smaller than 20 m (Figure 6). So, the parameterization formulas of K_α and K_T in Section 4.2 and 4.3 are mainly suitable for this range. At the same time, the floe sizes are mainly in this range for the marginal ice zone (Xie et al., 2013). Satellite optical data have been widely employed to retrieve MPF using remotely sensed surface reflectance according to the linear combination of different surface categories (Rösel et al., 2012). Zege et al. (2015) used the reflective properties of melt pond and sea ice to calculate the reflectance of ice floe through linear combination, and then retrieve the MPF and albedo, which is called the Melt Pond Detector (MPD) algorithm. This algorithm was shown to slightly overestimate MPF compared to field data. The MPD algorithm also obviously overestimated the MPF compared to

https://doi.org/10.5194/egusphere-2023-1758
Preprint. Discussion started: 8 August 2023

the airborne-classified ponds over FYI (Istomina et al., 2015). So did the Rösel et al. (2012), who also took the satellite optical data. The larger the MPF, the easier it is for solar radiation to penetrate into the lateral ocean and consequently produce a larger difference. For example, as MPF increases, the retrieved MPF is obviously larger than that obtained from in situ measurements in Fig.8 of Xiong and Ren (2023). At different latitudes and pond evolution stages, parameterization results can assist in correcting the field observations got from linear combination and further retrieving the MPF by satellite optical data. If the reflectance calculated using satellite data by linear combination is larger than the actual values, then the retrieved MPF will be larger than the measured value to offset the error. Without considering the lateral transmission of the different MPF may be one reason for the overestimate of MPF.

5 Conclusion

A Monte Carlo model was employed to study the influence of melt pond and floe size on the AOPs of ice floe. The variation in AOPs and solar energy partitioning of floe were analysed based on predefined IOPs of sea ice and melt pond. The parameterization of K_α and K_T at different latitudes and pond formation stages were presented.

The results demonstrated that MPF and floe size have a strong effect on the AOPs of ice floe. An increase in MPF will significantly decrease the floe's albedo and increase T_b and Ψ_p. A decrease in ice floe size can obviously increase T_l and decrease the other AOPs at the same time. Two limiting cases with MPF = 100% and 0% at different d_i proved that the influence of T_l could be smaller than 3% when pond size or floe size reached 40 m. As floe size reached 200 m, the floe's AOPs were consistent with the results obtained with infinite medium. K_α and K_T were determined by the MPF and floe size. The increasing of floe size significantly decreased the K_α and K_T. As MPF increased, K_α increased and K_T decreased. The maximum K_α and K_T were lower than 1.07 with floe size 40 m, and when this reached 200 m, the two parameters were almost 1.0. MPF and floe size also affected the irradiance distribution and energy absorption rate. As floe size and MPF increased, more solar radiation penetrated the ocean bottom, especially for radiation within the 450 – 550 nm. The smaller the MPF, the larger the ice albedo.

Our study suggested that floe size plays an important role in determining the AOPs of melting ice. The K_α and K_T can vary with the latitude. Further, we proposed a parameterized formula to calculate K_α and K_T in the marginal ice zone. Different melting stages also has a great influence on K_α and K_T, especially for small-size floe (2 – 20 m). In addition to being affected by floe size, K_α and K_T are also closely related to MPF and H_i, respectively.

With the rapid melting of Arctic sea ice, floe sizes are getting increasingly smaller in the summer. Therefore, the influence of floe size on AOPs must be considered during investigations. The application of the plane-parallel hypothesis and linear combination will become increasingly challenging, which has also been highlighted in this study. For example, during the melting season, the linear combination will overestimate the albedo due to the effect of lateral transmission. However, the knowledge of solar irradiance distribution on floe obtained from in situ measurements is still limited. Further investigations of how solar energy is distributed to the melt pond bottom and lateral ice are still required.

Acknowledgements. This research was funded by the LiaoNing Revitalization Talents Program (XLYC2007033), the National Natural Science Foundation of China (41922045), and National Key Research and Development Program of China: 2019YFE197600.

Author contributions. HZ carried out the estimations and wrote the paper. MY, PL, JZ, QW, and ZL edited the paper. All co-authors discussed the results and edited the manuscript.

Data Availability Statement. The field data from melt pond evolution by Polashenski et al. (2012) are available at the Arctic Data Center: spectral albedos – Polashenski et al. (2016a); line photos – Polashenski et al. (2016b).

Competing interests. The authors declare that they have no conflict of interest.

References

Briegleb, B.P., Light, B.: A delta-eddington multiple scattering parameterization for solar radiation in the sea ice component of the community climate system model (No.NCAR/TN-472+STR). University Corporation for Atmospheric Research, http://doi.org/10.5065/D6B27S71, 2007.

Cao, X., Lu, P., Lei, R., Wang, Q., and Li, Z.: Physical and optical characteristics of sea ice in the Pacific Arctic Sector during the summer of 2018. Acta Oceanologica Sinica, 39 (9), 25-37, http://doi.org/10.1007/s13131-020-1645-6, 2020.

Flocco, D., Schroeder, D., Feltham, D.L., and Hunke, E.C.: Impact of melt ponds on Arctic sea ice simulations from 1990 to 2007. Journal of Geophysical Research: Ocean, 117 (C09032), http://doi.org/10.1029/2012JC008195, 2012.

Grenfell, T.C.: A radiative transfer model for sea ice with vertical structure variations. Journal of Geophysical Research: Ocean, 96 (C9), 16991-17001, http://doi.org/10.1029/91JC01595, 1991.

Grenfell, T. C., and Perovich, D. K.: Seasonal and spatial evolution of albedo in a snow-ice-land-ocean environment. Journal of Geophysical Research: Ocean, 109 (C01001), http://doi.org/10.1029/2003JC001866, 2004.

Grenfell, T.C., and Perovich, D.K: Incident spectral irradiance in the Arctic Basin during the summer and fall. Journal of Geophysical Research: Atmospheres, 113(D12117), http://doi.org/10.1029/2007JD009418, 2008.

Hudson, S.R., Granskog, M.A., Sundfjord, A., Randelhoff, A., Renner, A.H.H., and Divine, D.V.: Energy budget of first-year Arctic sea ice in advanced stages of melt. Geophysical Research Letters, 40, 2679-2683, http://doi.org/10.1002/grl.50517, 2013.

Istomina, L., Heygster, G., Huntemann, M., Schwarz, P., Birnbaum, G., Scharien, R., Polashenski, C., Rerovich, D., Zege, E., Malinka, A., Prikhach, A., Katsev, I.: Melt pond fraction and spectral sea ice albedo retrieval from MERIS data – Part 1:

https://doi.org/10.5194/egusphere-2023-1758
Preprint. Discussion started: 8 August 2023

Validation against in situ, aerial, and ship cruise data. The Cryosphere, 9 (4), 1551-1566, http://doi.org/10.5194/tc-9-1551-2015, 2015.

Katlein, C., Arndt, S., Nicolaus, M., Perovich, D.K., Jakuba, M.V., Suman, S., Elliott, S., Whitcomb, L.L., Mcfarland, C.J., Gerdes, R., Boetius, A., and German, C.R.: Influence of ice thickness and surface properties of light transmission through Arctic sea ice. Journal of Geophysical Research: Oceans, 120 (9), 5932-5944, http://doi.org/10.1002/2015JC010914, 2015.

Katlein, C., Arndt, S., Belter, H.J., Castellani, G., and Nicolaus, M.: Seasonal evolution of light transmission distributions through Arctic sea ice. Journal of Geophysical Research: Oceans, 124 (8), 5418-5435, http://doi.org/10.1029/2018JC014833, 2019.

Landy, J.C., Ehn, J.K., and Barber, D. G.: Albedo feedback enhanced by smoother Arctic sea ice. Geophysical Research Letters, 42 (24), 10714-10720, http://doi.org/10.1002/2015GL066712, 2015.

Liou K. An introduction to atmospheric radiation. Academic Press, 2002.

Light, B., Maykut, G.A., and Grenfell, T.C.: A two-dimensional Monte Carlo model of radiative transfer in sea ice. Journal of Geophysical Research: Oceans, 108 (C7), http://doi.org/10.1029/2002JC001513, 2003.

Light, B., Perovich, D.K., Webster, M. A., Polashenski, C., and Dadic, R.: Optical properties of melting first-year Arctic sea ice. Journal of Geophysical Research: Oceans, 120 (11), 7657-7675, http://doi.org/10.1002/2015JC011163, 2015.

Light, B., Smith, M.M., Perovich, D.K., Webster, M.A., Holland, M.M., Linhardt, F., Raphael, I.A., Clemens-Sewall, D., Macfarlane, A.R., Anhaus, P., and Bailey, D.A.: Arctic sea ice albedo: Spectral composition, spatial heterogeneity, and temporal evolution observed during the MOSAIC drift. Elementa-Science of Anthropocene, 10 (1), http://doi.org/10.1525/elementa.2021.000103, 2022.

Lu, P., Leppäranta, M., Cheng, B., and Li, Z.: Influence of melt-pond depth and ice thickness on Arctic sea-ice albedo and light transmittance. Cold Regions Science and Technology, 124, 1-10, http://doi.org/10.1016/j.coldregions.2015.12.010, 2016.

Lu, P., Cheng, B., Leppäranta, M., and Li, Z.: Partitioning of solar radiation in Arctic sea ice during melt season. Oceanologia, 60 (4), 464-477, http://doi.org/10.1016/j.oceano.2018.03.002, 2018.

Malinka, A., Zege, E., Istomina, L., Heygster, G., Spreen, G., Perovich, D., and Polashenski, C.: Reflective properties of melt ponds on sea ice. The Cryosphere, 12 (6), 1921-1937, http://doi.org/10.5194/tc-12-1921-2018, 2018.

Nicolaus, M., Katlein, C., Maslanik, J., and Hendricks, S.: Changes in Arctic sea ice result in increasing light transmittance and absorption. Geophysical Research Letters, 40 (11), 2699-2700, http://doi.org/10.1002/grl.50523, 2012.

Perovich D K.: The optical properties of sea ice. CRREL Monograph, 96-1, 25 pp., 1996.

Perovich, D.K., Grenfell, T.C., Light, B., Hobbs, P.V.: Seasonal evolution of the albedo of multiyear Arctic sea ice. Journal of Geophysical Research, 107 (C10), http://doi.org/10.1029/2000JC000438, 2002.

Perovich, D.K., Grenfell, T.C., Light, B., Elder, B.C., Harbeck, J., Polashenski, C., Tucker III, W.B., and Stelmach, C.: Transpolar observations of the morphological properties of Arctic sea ice. Journal of Geophysical Research: Oceans, 114 (C00A04), http://doi.org/10.1029/2008JC004892, 2009.

Perovich, D.K., Polashenski, C.: Albedo evolution of seasonal Arctic sea ice. Geophysical Research Letters, 39 (L08501), http://doi.org/10.1029/2012GL051432, 2012.

Petrich, C., Nicolaus, M., and Gradinger, R.: Sensitivity of the light field under sea ice to spatially inhomogeneous optical properties and incident light assessed with three-dimensional Monte Carlo radiative transfer simulations. Cold Regions Science and Technology, 73, 1-11, http://doi.org/10.1016/j.coldregions.2011.12.004, 2012.

Polashenski, C., Perovich, D., and Courville, Z.: The mechanisms of sea ice melt pond formation and evolution. Journal of Geophysical Research: Oceans, 117 (C01001), http://doi.org/10.1029/2011JC007231, 2012.

Rösel, A., Kaleschke, L., Birnbaum, G.: Melt ponds on Arctic sea ice determined from MODIS satellite data using an artificial neural network. The Cryosphere, 6 (2), 431-446, http://doi.org/10.5194/tc-6-431-2012, 2012.

Segelstein, D.: The complex refractive index of water, MS thesis, University of Missouri, Kansas City, available at: https://mospace.umsystem.edu/xmlui/handle/10355/11599 (last access: 1 May 2023), 1981.

Skyllingstad, E.D., Paulson, C.A., Perovich, DK.: Simulation of melt pond evolution on level ice. Journal of Geophysical Research: Oceans, 114 (C12019), http://doi.org/10.1029/2009JC005363, 2009.

Taylor, P.D., Feltham, D.L.: A model of melt pond evolution on sea ice. Journal of Geophysical Research: Oceans, 109 (C12007), http://doi.org/10.1029/2004JC002361, 2004.

Wang, M., Su, J., Landy, J., Leppäranta, M., Lei, G.: A new algorithm for sea ice melt pond fraction estimation from high-resolution optical satellite imagery. Journal of Geophysical Research: Oceans, 125 (10), http://doi.org/10.1029/2019JC015716, 2020.

Webster, M.A., Rigor, I.G., Perovich, D.K., Richter-Menge, J.A., Polashenski, C.M., and Light, B.: Seasonal evolution of melt ponds on Arctic sea ice. Journal of Geophysical Research: Oceans, 120 (9), 5968-5982, http://doi.org/10.1002/2015JC011030, 2015.

Webster, M.A., Holland, M., Wright, N.C., Hendricks, S., Hutter, N., Itkin, P., Light, B., Linhardt, F., Perovich, D.K., Raphael, I.A., Smith, M.M., Albedyll, L., Zhang, J.: Spatiotemporal evolution of melt ponds on Arctic sea ice: MOSAiC observations and model results. Elementa-Science of The Anthropocene, 10 (1): https://doi.org/10.1525/elementa.2021.000072, 2022.

Xie, H., Lei, R., Ke, C., Wang, H., Li, Z., Zhao, J., and Ackley, S.F.: Summer sea ice characteristics and morphology in the Pacific Arctic sector as observed during the CHINNARE 2010 cruise. The Cryosphere, 7 (4), 1057-1072, http://doi.org/10.5194/tc-7-1057-2013, 2013.

Xiong, C., Ren, Y.: Arctic sea ice melt pond fraction in 2000-2021 derived by dynamic pixel spectral unmixing of MODIS images. ISPRS Journal of Photogrammetry and Remote Sensing, 197, 181-198, http://doi.org/10.1016/j.isprsjprs.2023.01.023, 2023.

Yu, M., Lu, P., Cheng, B., Leppäranta, M., and Li, Z.: Impact of microstructure on solar radiation transfer within sea ice during summer in the Arctic: a model sensitivity study. Frontiers in Marine Science, 9 (861994), http://doi.org/10.3389/fmars.2022.861994, 2022.

https://doi.org/10.5194/egusphere-2023-1758
Preprint. Discussion started: 8 August 2023

Zege, E., Malinka, A., Katsev, I., Prikhach, A., Heygster, G., Istomina, L., Birnbaum, G., and Schwarz, P.: Algorithm to retrieve the melt pond fraction and the spectral albedo of Arctic summer ice from satellite optical data. Remote Sensing of Environment, 163, 153-164, http://doi.org/10.1016/j.rse.2015.03.012, 2015.

Zhang, J., Schweiger, A., Webster, M., Light, B., Steele, M., Ashjian, C., Campbell, R., Spitz, Y.: Melt pond conditions on declining Arctic sea ice over 1979 – 2016: Model development, validation, and results. Journal of Geophysical Research: Oceans, 123 (11), 7983-8003, http://doi.org/10.1029/2018JC014298, 2018.

Zhang, H., Yu, M., Lu, P., Zhou, J., Xie, F., Wang, Q., Li, Z.: Experimental investigation of partitioning of radiation in the melt pond-ice-ocean system. Cold Regions Science and Technology, Under Review, 2023.